Insights on the Electrochemical Activity of Porous Carbonaceous Electrodes in Non-Aqueous Vanadium Redox Flow Batteries

As Published: 10.1149/2.0621714JES

Publisher: The Electrochemical Society

Persistent URL: https://hdl.handle.net/1721.1/134874

Version: Final published version: final published article, as it appeared in a journal, conference proceedings, or other formally published context

Journal of The Electrochemical Society, **164** (14) A3673-A3683 (2017)
0013-4651/2017/164(14)/A3673/11/$37.00 © The Electrochemical Society

Insights on the Electrochemical Activity of Porous Carbonaceous Electrodes in Non-Aqueous Vanadium Redox Flow Batteries

Ibrahim Mustafa,[a] Musbaudeen O. Bamgbopa,[a] Eman Alraeesi,[a] Yang Shao-Horn,[b] Hong Sun,[c] and Saif Almheiri[a,d,z]

[a]*Department of Mechanical Engineering, Khalifa University of Science and Technology, Masdar Institute, Masdar City, Abu Dhabi, United Arab Emirates*
[b]*Electrochemical Energy Laboratory, Department of Materials Science & Engineering, Massachusetts Institute of Technology, Cambridge, Massachusetts 02139, USA*
[c]*School of Transportation Engineering, Shenyang Jianzhu University, Shenyang 110168, People's Republic of China*
[d]*Division of Engineering Technology and Science, Higher Colleges of Technology, United Arab Emirates*

Porous carbonaceous electrodes have the potential utility as electrodes for non-aqueous VRFBs due to being inexpensive, chemically stable, and electrochemically active. In this work, we provide insights on the electrochemical kinetics of $[V(acac)_3]^0/[V(acac)_3]^+$ and $[V(acac)_3]^0/[V(acac)_3]^-$ redox reactions at freestanding sheets of multiwalled carbon nanotubes (MWCNTs), or buckypapers (BPs), and graphitized carbon fiber-based nonwovens papers (CPs). The use of freestanding sheets eliminates the need for a metal substrate; thus, the true electrochemical response at these electrodes is measured. Even though porous carbonaceous electrodes provide high surface area for the electrochemical reaction, their porous nature poses a fundamental challenge caused by thin-film-like diffusion process; leading to a marked ohmic resistance within the pores of the electrodes. Higher current densities are obtained with the BP electrode due to their larger surface area in comparison to the CP electrode; however, the BP electrode show less efficient kinetic facility for the investigated redox couples as evident by electrochemical impedance spectroscopy and polarization curves results. Charge–discharge cycling demonstrates that porous carbonaceous electrodes may require various treatments to modify the surface chemistries to obtain improved cycling efficiencies.

Manuscript submitted August 24, 2017; revised manuscript received November 13, 2017. Published December 1, 2017.

The global demand for energy has been forecasted to reach 860 exajoules by 2040,[1] and this increase will, in turn, require a concomitant increase in energy storage capacity. Redox flow batteries (RFBs) have the potential to be a promising solution for large-scale energy storage.[2] The first RFB was proposed by NASA in the 1970s,[3] used iron–chromium redox chemistry, and since then RFBs with a variety of active redox species and solvents have been established.[4,5] The RFBs reported to date exhibit different efficiencies, kinetics, potential windows, operating constraints, voltages, and costs. Generally speaking, flow battery redox chemistry fall into three main groups: (1) aqueous RFBs, of which the most notable are the V/V,[6] Zn/Br,[7] Fe/V,[8] and Zn/Ce[9] systems, (2) non-aqueous RFBs (NARFBs), of which the most notable are the $V(acac)_3$ (acac = acetylacetonate),[10] $Cr(acac)_3$,[11] $Mn(acac)_3$,[12] $Ru(bpy)_3$ (bpy = 2,2′-bipyridine),[13] $Co(bpy)_3$,[14] $Fe(bpy)_3$,[15] and all-organic systems,[16] and (3) semi-solid flow batteries, of which the most notable are the $LiCoO_2$/Li,[17] $LiTi_2(PO_4)_3$/$LiFePO_4$,[18] Li-PS/Li,[19] Si-C/Li,[20] S-C/Li,[21] $Na_xNi_{0.22}Co_{0.11}Mn_{0.66}O_2$/$NaTi_2(PO_4)_3$,[22] TEMPO/viologen,[23] LiL-S/C,[24] Li/O_2,[25] all of which have been extensively reviewed in the literature.[4,26–30]

Aqueous all-vanadium RFBs (VRFBs), first suggested in 1985 by Skyllas-Kazacos et al.,[31,32] are the most developed, having low crossover rates, reasonable energy densities (20–35 Wh L^{-1}),[33,34] reasonable cell peak power densities ($\leq$1340 mW cm^{-2}),[35–38] and high energy efficiencies (EE > 80%).[34,39–42] To further increase flow battery energy and power densities, researchers have replaced aqueous electrolytes with non-aqueous electrolytes, allowing a high-voltage operation per cell. For example, Liu et al. developed a non-aqueous VRFB[10] with a cell potential of 2.2 V and thus can potentially offer energy densities higher than those of aqueous VRFBs,[28] where $[V(acac)_3]^0/[V(acac)_3]^+$ and $[V(acac)_3]^0/[V(acac)_3]^-$ were used as active redox couples (Equations 1 and 2) in tetraethylammonium tetrafluoroborate ($TEABF_4$) based electrolyte.

$$\text{Positive Side: } \left[V(acac)_3\right]^0 - e^- \leftrightarrow \left[V(acac)_3\right]^+$$
$$E^o = 0.4 \text{ V vs } Ag/Ag^+ \quad [1]$$

$$\text{Negative Side: } \left[V(acac)_3\right]^0 + e^- \leftrightarrow \left[V(acac)_3\right]^-$$
$$E^o = -1.8 \text{ V vs } Ag/Ag^+ \quad [2]$$

[z]E-mail: salmheiri@masdar.ac.ae

Most of the studies on non-aqueous VRFBs involved investigations of the solvent and the membrane,[43–47] whilst fewer studies explored the kinetics of the $[V(acac)_3]^0/[V(acac)_3]^+$ and $[V(acac)_3]^0/[V(acac)_3]^-$ redox reactions at the electrodes. Electrode studies are important to explore the greater opportunities that lie within NARFBs. Different materials have different morphological and electrochemical properties toward certain redox couples, and thus will facilitate reactions at different rates, directly impacting the amount of energy that can be utilized per ion species at the electrode/electrolyte interface, and in turn, can significantly affect the attainable power densities and operational efficiencies of the battery. Liu et al.[10] demonstrated that the $[V(acac)_3]^0/[V(acac)_3]^+$ and $[V(acac)_3]^0/[V(acac)_3]^-$ redox reactions (with a $TEABF_4$ in acetonitrile electrolyte) at a glassy carbon electrode (GCE) were quasi-reversible, however, charge discharge cycling showed low coulombic efficiencies (≈50%) which was attributed to the possibility of side reactions and/or significant crossover. In contrast, Shinkle et al.[48] suggested that both redox couples showed Nernstian reversible behavior on glassy carbon, gold, and platinum electrodes, whereas the gold electrode showed the highest attainable peak currents at a given scan rate. The calculated exchange current densities were highest for the gold electrode (8.4 Am^{-2}), as compared with the glassy carbon (1.3 Am^{-2}) and the platinum electrode (3.8 Am^{-2}). The authors suggested that the improvement in reaction rates achieved with gold was not significant, and could be surpassed by using high surface area carbon electrodes. Moreover, a more recent study by Zhang et al.[49] suggested a quasi-reversible behavior with a glassy carbon electrode toward the $[V(acac)_3]^0/[V(acac)_3]^+$ and $[V(acac)_3]^0/[V(acac)_3]^-$ redox couple (with either tetrabutylammonium hexafluorophosphate or 1-ethyl-3-methyl imidazolium hexafluorophosphate in acetonitrile electrolytes), and the results highlighted that the improvement in reversibility of the redox reactions was attributed to the enhancement in diffusion coefficients attainable through the use of the 1-ethyl-3-methyl imidazolium hexafluorophosphate supporting electrolyte. Tables I and II summarize the previous works performed with various electrode types for non-aqueous VRFBs.

Other researchers have investigated the use of non-vanadium active species for NARFBs with various electrode materials, and suggested that improvements in performance are attainable through the use of carbonaceous materials; Park et al.[14] investigated the effects of coating metal electrodes with various carbon materials (carbon

Table I. The performance of different electrodes reported in the literature from selected charge–discharge experiments for non-aqueous VRFBs.

Electrode/Size	Cell Setup	$j_{charge}/j_{discharge}$	Membrane	Electrolyte in each side	CE (%)	EE (%)	Ref.
GE/15 × 3 × 25 mm	H-Cell	0.1 to 1.0 mA/ 0.1 to 1.0 mA	AMI-7001	15 ml of 0.01 M $V(acac)_3$/ 0.5 M $TEABF_4$	32 for charge and 47 for discharge	-	10
GE/80 × 15 × 5 mm	H-cell	1 mA/ 0.1 mA	AMI-7001	15 ml of 0.01 M $V(acac)_3$/0.2 M $TEAPF_6$	53.31, 57.44 (at cycles 3, 4)	-	49
GE/80 × 15 × 5 mm	H-cell	1 mA/ 0.1 mA	AMI-7001	15 ml of 0.01 M $V(acac)_3$/0.2 M $EMIPF_6$	46.04, 43.46 (at cycles 3, 4)	-	49
GE/a = 7 cm^2	H-cell	0.14 mA cm^{-2} /0.014 mA cm^{-2}	Neosepta AHA	10 ml of 0.05 M $V(acac)_3$/ 0.5 M $TEABF_4$	70,73 (at cycles 10, 11)	34 (at cycles 10, 11)	75
CP/a = 5 cm^2	Zero-gap RFB with flow rate at 25 mL min^{-1}	10 mA cm^{-2} /10 mA cm^{-2}	Nafion	25 ml of 0.1 M $V(acac)_3$/ 0.5 M $TEABF_4$	91 (at cycle 5)	80 (at cycle 5)	76
			Daramic		74 (at cycle 5)	68 (at cycle 5)	
			Neosepta		51 (at cycle 5)	26 (at cycle 5)	
CF/a = 5.65 cm^2	Flow-through with flow rate at 25 mL min^{-1}	10 mA cm^{-2} /10 mA cm^{-2}	Nafion	25 ml of 0.1 M $V(acac)_3$/ 0.5 M $TEABF_4$	90 (at cycle 5)	83 (at cycle 5)	76
			Daramic		81 (at cycle 5)	75 (at cycle 5)	

Abbreviations: *j*, applied current; CE, coulombic efficiency; EE, energy efficiency; GE, graphite electrode; CP, carbon paper; CF, carbon felt. A dash (–) indicates that the information was not reported in or could not be deduced from the reference.

black, carbon nanofiber, and graphene) toward the $[Co(bpy)_3]^{+/2+}$ and $[Fe(bpy)_3]^{2+/3+}$ redox couples, and found that the highest peak current was given by the electrodes coated with carbon black, which was about 2 times larger than that attainable by the bare metal electrode, and was attributed to the higher surface area offered by the carbon coating. The electrochemical activity of carbon nanotubes (CNTs) toward the same redox couples were also investigated by Lee et al. through the modification of Ni foam electrodes with both bare and functionalized CNTs.[50] Out of all the investigated electrodes, those modified with nitrogen-doped CNTs showed the lowest charge transfer resistances and the highest electrochemical active surface areas which consequently resulted in the highest electrochemical reversibility, and the highest attainable efficiencies during charge discharge experiments (VE ≈ 92% and EE ≈ 80%), as compared to those obtained by pure Ni foam electrodes (VE ≈ 86% and EE ≈ 74%), and the non-doped CNT electrodes (VE ≈ 90% and EE ≈ 76%). This behavior was attributed to the large surface area provided by the CNTs and the presence of defect sites made available by the nitrogen functional groups, which in turn improved the kinetics of the redox reactions and facilitated mass transfer at the electrode/electrolyte interface. Another carbonaceous material that has been explored by researchers is graphene due to its impressive electronic conductivity and electrochemical activity.[51] Lee et al.[52] investigated the effects of utilizing 3D graphene multilayers grown on Ni-foam toward the $[Co(bpy)_3]^{+/2+}$ and $[Fe(bpy)_3]^{2+/3+}$ redox couples, and have demonstrated that the electrode's activity was improved in terms of both peak current and peak separation during their cyclic voltammetry tests, with an increase in the standard rate constants (k^o) when 3D graphene multilayers were present on the electrode. Moreover, their flow cell tests demonstrated high efficiencies (VE ≈ 91%, and EE ≈ 82%) attainable with the 3D graphene modified Ni-foam electrodes, which was up to 8% higher than that demonstrated by the flow cell without the graphene multilayers. The improvement in performance was attributed to the 3D graphene multilayer composing of many defects thus enhancing the charge transfer at the electrode/electrolyte interface, and increasing the number of electrochemically active sites available for the reaction. Recently, Bamgbopa et al.[53] demonstrated carbon paper electrode performances toward the acetylacetonate-based Fe_3/Fe_2 and Cr_3/Cr_2 redox couples, and illustrated high peak separations which were attributed to the porous nature of the electrode. Moreover, they demonstrated a Fe/Cr NARFB flow cell performance utilizing carbon paper electrodes (CE ≈ 99%, VE ≈ 53%, EE ≈ 53%).

Porous carbonaceous electrodes have the potential utility as electrodes for non-aqueous VRFBs due to being inexpensive, chemically stable, and electrochemically active. The brief review of the literature shows that, in general, researchers investigated two types of carbon-based electrodes in NARFBs: (a) planar electrodes (e.g. GCE), and (b) metal foam electrodes modified with carbonaceous materials (e.g. Ni/CNTs). Carbonaceous planar electrodes do not offer enough surface area for real battery applications, and the electrochemical reaction at a metal foam modified with CNTs is likely to be influenced by the effects of mixed kinetics due to the presence of more than one active electrode material. Thus, in this work, we provide insights on the electrochemical kinetics of $[V(acac)_3]^0/[V(acac)_3]^+$ and $[V(acac)_3]^0/[V(acac)_3]^-$ redox reactions at porous carbon-based electrodes in the form of freestanding sheets; thus, eliminating the

Table II. The performance of selected electrodes reported in the literature from cyclic voltammetry experiments, performed at room temperature, utilizing 0.01 M $V(acac)_3$ species dissolved in acetonitrile.

Electrode	Supporting Electrolyte	D ($\times 10^{-6}$ cm^2 s^{-1})	i_o (A m^{-2})	Ref.
GCE	0.5 M $TEABF_4$	1.8–2.9	-	10
Ag	0.05 M $TEABF_4$	3.93	8.4	48
GCE	0.05 M $TEABF_4$		1.3	
Pt	0.05 M $TEABF_4$		3.8	
GCE	0.5 M $TEABF_4$	0.92–1.47	-	49
	0.5 M $EMIPF_6$	2.35–3.79		

Abbreviations: *D*, Diffusion coefficient; i_0, exchange-current density; A dash (–) indicates that the information was not reported in or could not be deduced from the reference.

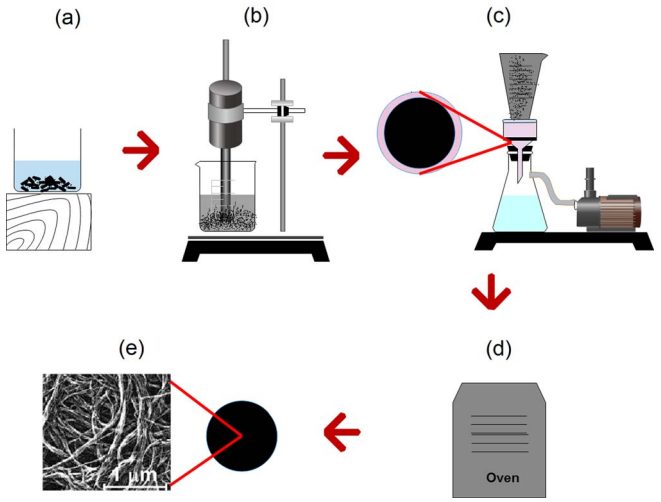

Figure 1. (a) MWCNTs in aggregate form (bundles) were added to a small volume of DI water. (b) Sonication was used to de-agglomerate the MWCNTs with the addition of DI water to increase the system volume to the desired level. (c) The resulting suspension of homogeneously dispersed MWCNTs in DI water was vacuum-filtered through a nylon membrane filter to separate the MWCNTs from the solution. (d) The wet BP was peeled from the filter paper and vacuum-dried at 80°C. (e) A high-surface-area, high-electrically-conductive BP electrode consisting of entangled MWCNTs was obtained.

need for an underlaying metal substrate.[54,55] In particular, we explore the effects of surface area utilization and the nature of the porous structure of multiwalled carbon nanotube (MWCNT) sheets, or buckypapers (BPs), and compare the results with those of a commercially available graphitized carbon fiber-based nonwoven paper (CP) electrode. In addition, we evaluate the performance of the two types of electrodes in a flow-cell assembly with an electrolyte consisting of $V(acac)_3$ and $TEABF_4$ in acetonitrile.

Experimental

Chemicals.—Acetonitrile (anhydrous 99.8%, Sigma-Aldrich) was dried over activated 3 Å molecular sieves. $TEABF_4$ (99%) and $V(acac)_3$ (97%) were obtained from Sigma-Aldrich. Aqueous solutions were prepared with ultrapure DI water (Resistivity > 18.2 MΩ × cm, Purite Select Fusion).

Electrode preparation.—A commercially available CP electrode (SGL 10AA, SGL Carbon) was used in this study. Prior to use, the CP electrode was sonicated in a 50% nitric acid bath for 10 min, thoroughly rinsed in high-purity DI water, and then dried at 80°C under vacuum for 8 h. The dried electrode was then transferred to a glove box and soaked in the support solution (0.05 M $TEABF_4$ in acetonitrile) for at least 4 h prior to use.

A BP electrode, in the form of a freestanding sheet of MWCNTs, was fabricated by means of a vacuum filtration technique as follows (Fig. 1). MWCNT flakes produced by means of chemical vapor deposition consisting of strands with diameters ranging from 4 to 14 nm and an average length of 30 μm,[56] were obtained from Applied Nanostructured Solutions (USA).[57] The MWCNTs (0.60 g) were dispersed in 50 mL of DI water and sonicated for 10 min at a power of 30 W. Then the volume of the suspension was increased to 100 mL with DI water, and the suspension was sonicated for 100 min with pulsation (on/off ratio, 20:30). Then the suspension volume was increased to 600 mL with DI water, and the suspension was sonicated for 10 min at 30 W. The resulting stable suspension of MWCNTs was vacuum-filtered through a nylon membrane filter (Whatman filter paper, 45 μm pore size, 47 mm diameter) by means of a diaphragm pump (Gast Manufacturing). The wet BP electrode was peeled off the filter paper and dried in a vacuum oven at 80°C for 8 h.

Morphological and physical characterization of the electrodes.—The morphology of the electrodes was investigated by means of field emission scanning electron microscopy (SEM, FEI Quanta 250). SEM images were obtained by probing the sample at a working distance of 10 mm, under high vacuum. Electrical conductivity at room temperature was measured by means of a four-probe technique with a digital multimeter (Keysight 34465A). Physisorption of nitrogen gas was measured at 77 K with a surface area analyzer (Quantachrome Nova 2000e). The samples were first degassed at 200°C for 6 h, and then the surface area was estimated by means of a multipoint Brunauer–Emmett–Teller (BET) technique; the values acquired over the linear region (P/P_0 = 0–0.35) of the adsorption isotherm. Fourier transform infrared (FTIR) transmittance spectra were obtained between the wavelength range of 500 and 4000 cm^{-1} using a FTIR detector under liquid nitrogen with a spectrometer (VERTEX 80 V, Bruker), and the FTIR samples were prepared by creating pellets of KBr and the sample in a mass ratio of 100:1.

Electrochemical characterization.—Electrochemical characterizations were conducted with a Parstat MC potentiostat (Princeton Applied Research). All experiments were performed in an argon-filled glove box (MBRAUN LABstar) at room temperature. Cyclic voltammetry (CV) and electrochemical impedance spectroscopy (EIS) were performed in a three-electrode-cell configuration with a Ag/Ag^+ reference electrode (prepared from 0.1 M $AgNO_3$ and 0.1 M supporting electrolyte in acetonitrile) and a graphite foil (1.5 cm^2, 99.8%, Alfa-Aesar) counter electrode. The voltage drop due to internal resistance (iR) was compensated for during CV acquisition using an automatic method (MC Parstat iR drop compensation based on positive feedback), and using a manual method (obtained from the high frequency region using EIS). Electrochemical impedance spectroscopy (EIS) measurements were performed at the equilibrium potentials of the positive and the negative electrolytes with an amplitude of 10 mV RMS, over a frequency range between 10 kHz and 0.01 Hz. Throughout the experiments, the geometric area of the working electrode was maintained at 0.1 cm^2, and was about 1/15 that of the area of the counter electrode. The electrolyte consisted of 0.01 M $V(acac)_3$ as the active species and 0.05 M $TEABF_4$ as the supporting electrolyte in acetonitrile.

For discharge polarization curve and charge discharge cycling performance testing, we used a flow-cell assembly (Fuel Cell Technologies) with an electrolyte consisting of 0.05 M $V(acac)_3$ and 0.2 M $TEABF_4$ in acetonitrile. The assembly had a working area of 5 cm^2 and a single serpentine flow channel. The tank on each side of the flow-cell assembly contained 25 mL of electrolyte. A single type of electrode, either CP or BP, was used in each half-cell of a two-electrode configuration. The total exposed geometric electrode area for the flow cell was 10 cm^2. The electrolyte from the tanks was circulated through the cell by means of a pair of peristaltic pumps (Masterflex) at a rate of 30 mL min^{-1}.

NafionSi membranes were utilized and were prepared as described in literature[44,58,59]. To summarize, Nafion 115 membranes (DuPont) were heated in 0.5 M aqueous sulfuric acid at 70°C for 2 h to convert them to the H^+ conducting form. Afterward, the membranes were rinsed and then soaked in DI water for another 1 h at 70°C to remove excess acid. The resulting H^+-forms of the membranes were then neutralized using a 1 M methanolic aqueous solution tetrabutylammonium hydroxide, at room temperature for 18 h. The membranes were then soaked in a solution of methanol:DI water (5:1) at room temperature overnight, and a mixture of tetraethylorthosilicate (TEOS) – methanol was added to achieve a solution of DI water:TEOS (4:1 ratio) under stirring. After 3 minutes, the membrane was soaked in methanol to remove any excess reactants on its surface, and was then vacuum-dried for 24 h, before being transferred to a glove box, in which it was equilibrated in a 0.1 M solution of $TEABF_4$ (which

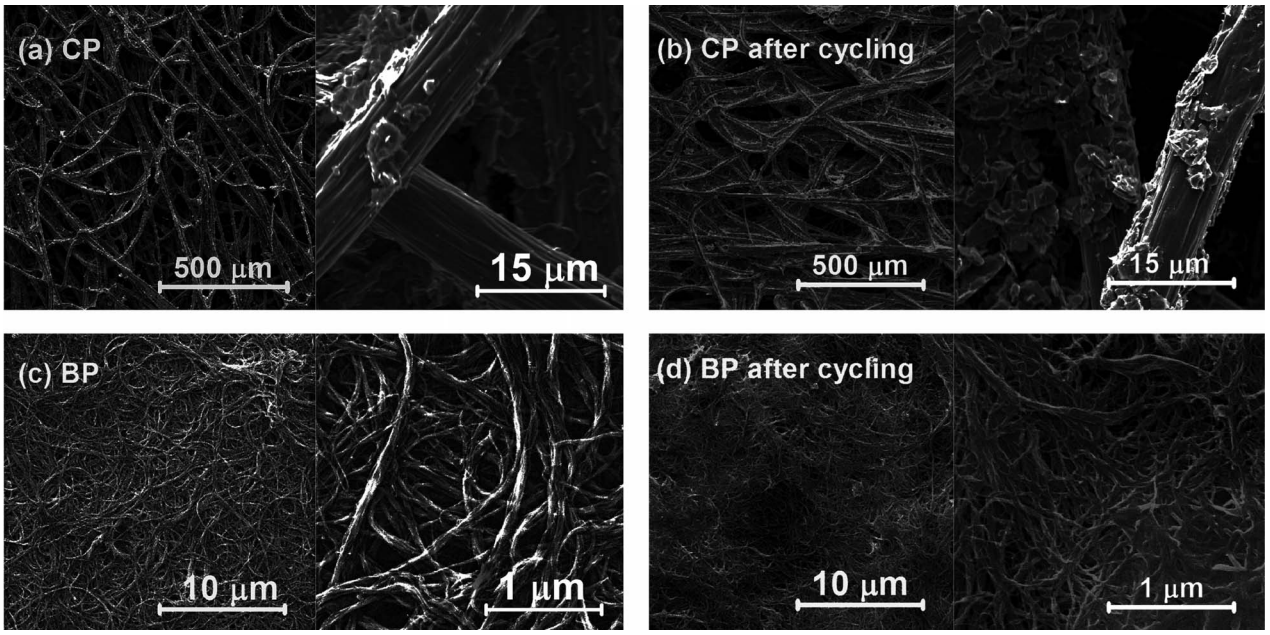

Figure 2. Field emission SEM images of (a) a CP electrode and (b) a CP electrode after charge discharge in a flow cell for 50 cycles at 50 mA cm^{-2}, and images for (c) our in-lab fabricated BP electrode, and (d) a BP electrode after charge discharge in a flow cell for 50 cycles at 25 mA cm^{-2}, probed at various magnifications. The closely packed strands of the BP electrode gave it a larger surface area than that of the CP electrode. After cycling, both electrodes maintained their 3-dimensional entangled network of carbon fibers, but were more closely packed and agglomerated (with the presence of active species residue) as compared with the as received samples. The effect was more predominant for the BP electrode as compared with the CP electrode.

contained the corresponding TEA^+) in acetonitrile for at least 3 days prior to use.

Results and Discussion

Morphological and physical characterization of the electrodes.— *Microscopy.*—The morphologies of the commercially available CP electrode and our in-lab fabricated BP electrode were compared by SEM at various magnifications (Figs. 2a, 2c). Although both electrodes consisted of a three-dimensional network of entangled carbon fibers, the strands in the BP electrode were more closely packed and consisted of smaller fiber diameters (8 to 12 nm) as compared to that of the CP electrode (10 μm), giving the BP electrode a larger surface area than that of the CP electrode. Furthermore, a large proportion of the surface area of the fibers in the CP electrode were occupied with carbon filler structures, which further contributed to their reduced surface area. The BP electrode had a smaller thickness (250 μm), an aerial weight (34.6 g m^{-2}) a much larger BET surface area (190 m^2 g^{-1} $\simeq$ 0.657 m^2 cm^{-2}) and a higher electrical conductivity (5.5 × 10^3 S m^{-1}) as compared with the CP electrode (280 μm, 85 g m^{-2}, 1.8 m^2 g^{-1} $\simeq$ 0.015 m^2 cm^{-2}, and 3.1 × 10^3 S m^{-1}), indicating that the BP electrode could be expected to have a high electrochemical surface area. Moreover, SEM images for the electrodes (Figs. 2b, 2d) after charge discharge cycling show that the networks of carbon fibers remain 3-dimensional and entangled for both electrodes after cycling, but the individual carbon fibers become more agglomerated (with the presence of active species residue) for both electrodes, which can be a contributor to the effects of mass transport resistance on resulting capacity decay. This agglomeration was more predominant in the cycled BP electrode as compared with the cycled CP electrode as expected, because the BP fibers are more closely packed.

FTIR analysis.—The functional groups on both the CP and BP electrodes were characterized using FTIR (Fig. 3). Recall that both electrodes were dried under vacuum for 8 h to eliminate the presence of any water or humidity. For the CP electrode, the peak at 3454 cm^{-1} was attributed to the stretching vibration of –OH bond. The peaks at 1377 and 1080 cm^{-1} were attributed to the bending vibration of –CH and C-O respectively. Similarly, the BP electrode exhibited a peak at 3436 cm^{-1} which was attributed to the stretching vibration of –OH bond, and peaks at 1388, and 1089 cm^{-1} which were attributed to the bending vibration of –CH and C-O respectively. The results suggest that both electrodes had a similar surface chemistry.

Electrochemical characterization.— *Cyclic voltammetry.*—We recorded the cyclic voltammograms of the CP and BP electrodes in an acetonitrile solution of 0.01 M $V(acac)_3$ as the active species and 0.05 M $TEABF_4$ as the supporting electrolyte at various scan rates (Figs. 4a, 4b and 4c, 4d, respectively). The voltammograms showed the $[V(acac)_3]^0/[V(acac)_3]^-$ and $[V(acac)_3]^0/[V(acac)_3]^+$ peaks indicating the electrode activities toward the negative and positive redox

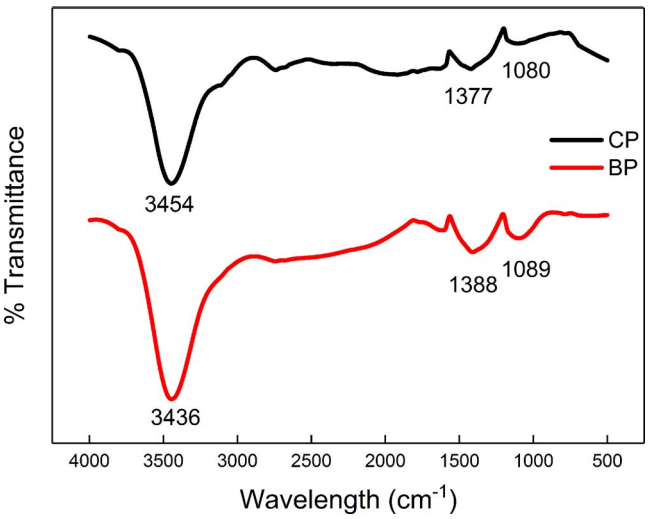

Figure 3. FTIR spectra for the CP and BP electrodes. Both electrodes had a similar surface chemistry.

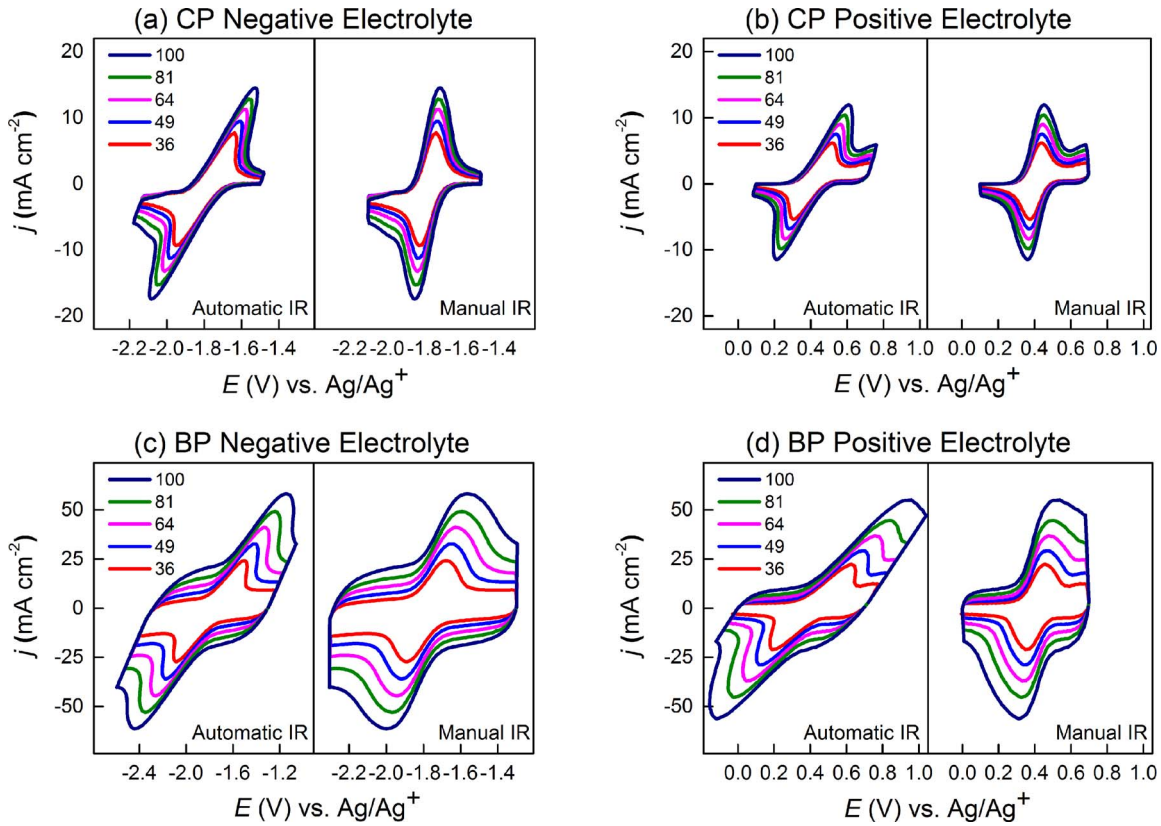

Figure 4. iR-corrected cyclic voltammograms recorded at various scan rates for an acetonitrile solution of $V(acac)_3$ (0.01 M) and $TEABF_4$ (0.05 M) at room temperature: (a, b) CP electrode and (c, d) BP electrode. Even though the cyclic voltammograms were compensated for iR losses, the voltammograms are still skewed due to the large iR losses in the cell. The insets show the non-skewed voltammograms obtained when manual iR compensation was performed.

couples, respectively. Both the peak separation and the peak current increased with increasing scan rate. Even though the cyclic voltammograms were compensated for iR losses, the voltammograms are still skewed due to the large iR losses in the cell that were uncompensated for by the potentiostat.

Unlike those obtained with CP and BP electrodes, the voltammograms (Fig. 5) at a GCE show the typical behavior of iR-compensated voltammograms; i.e. non-slanted voltammograms. To answer why the CP and BP still showed skewed voltammograms even after iR compensation, we turned into investigating the mode of mass transfer. Because CP and BP electrodes are porous in nature, it is expected that the mode of mass transfer is a combination of semi-infinite planar diffusion toward the electrode surface and thin layer diffusion within the porous structure.[60] We believe that the thin layer diffusion process is responsible for the slanted voltammograms because the local

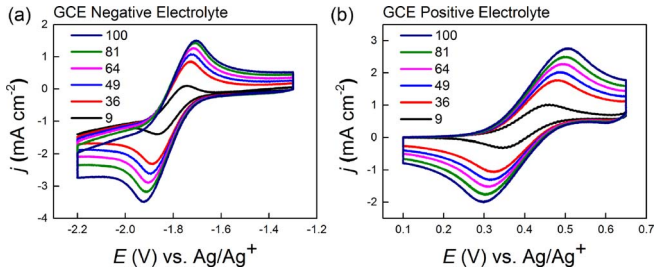

Figure 5. iR-corrected cyclic voltammograms at a GCE recorded at various scan rates for an acetonitrile solution of $V(acac)_3$ (0.01 M) and TEABF4 (0.05 M) at room temperature in the (a) negative electrolyte and the (b) positive electrolyte. Three electrode setup was used with GCE working, graphite foil counter and Ag/Ag+ reference electrodes. Notice the typical shape for iR compensated voltammograms in comparison to Fig. 4.

concentration of the supporting electrolyte within the pores is much lower than that of the bulk electrolyte;[61] thus, we suspect that the electrolyte resistance in the pores is substantially high leading to the skewed voltammograms seen with CP and BP electrodes. Based on the shape of the voltammograms of the planar GCE and the porous electrodes, it appears that automatic iR compensation was successful in accounting for the electrolyte resistance between the reference electrode and the surface of the working electrode; but was not able to account for the electrolyte resistance resulted from thin layer diffusion occurring within the pores of the CP and BP electrodes. Moreover, as shown in the SEM images, because the porous structure in the BP electrode is more closely packed than that of the CP electrode, we expect that the effect of thin layer diffusion within the BP electrode is markedly higher than the CP electrode. This is evident by the more skewed voltammograms of the BP electrode in comparison to the CP electrode; thus, the electrolyte resistance within the BP electrode is higher than that of the CP electrode.

There is a limit on how much iR compensation can be done due to the inherently high resistance of non-aqueous electrolytes.[62–64] Increasing the concentration of the supporting electrolyte will certainly reduce the electrolyte resistance within the pores of the electrodes; however, this will come at the expense of affecting the solubility of the active species. The insets in Fig. 4 show that skewed-free voltammograms could be obtained if manual iR compensation is performed. Moreover, we were limited by the potential window of the electrolyte, thus we have performed CVs within the respective potential ranges and up to a scan rate of 100 mV s^{-1} because peak separations can become sufficiently high at higher scan rates, and can approach electrolyte degradation potentials. Thus, moving forward, we based our electrochemical analyses on the insets of Fig. 4 (manual iR compensation) for demonstration purposes only.

Comparison of the voltammograms obtained at a scan rate of 36 mV s^{-1} (Figs. 6a, 6b) clearly revealed that the peak current

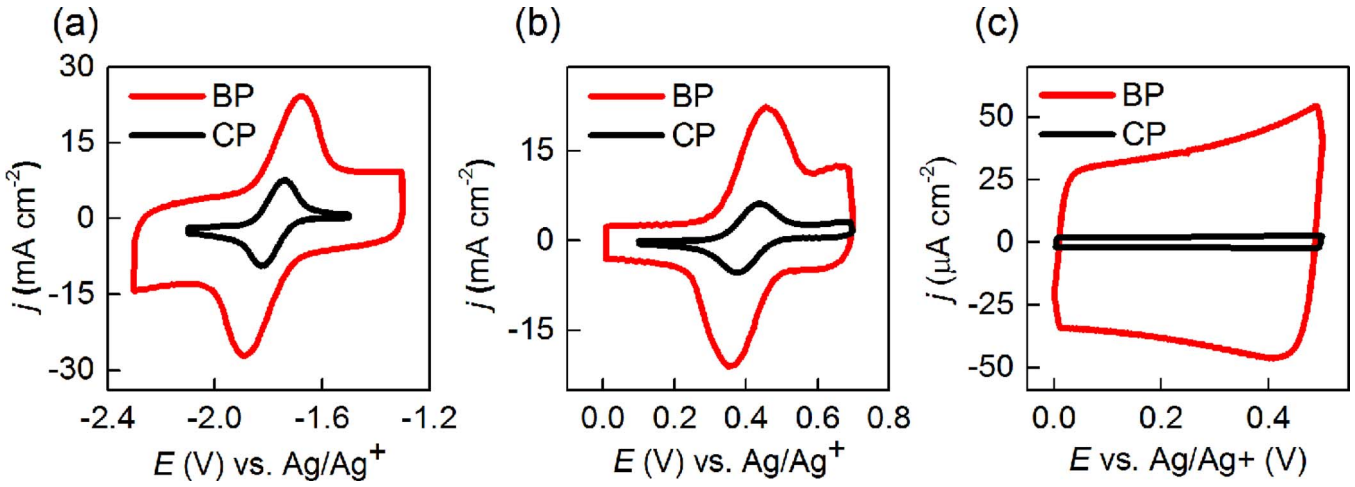

Figure 6. (a,b) Cyclic voltammograms recorded for the CP and BP electrodes at a scan rate of 36 mV s^{-1} in an acetonitrile solution of $V(acac)_3$ (0.01 M) and $TEABF_4$ (0.05 M) at room temperature scanned for the (a) negative and (b) positive redox couples. The voltammograms clearly show that the faradaic currents attainable with the BP electrode were higher than those attainable with the CP electrode. (c) Cyclic voltammograms recorded for the BP and the CP electrodes at a scan rate of 25 mV s^{-1} in an acetonitrile solution of 0.05 M $TEABF_4$, indicating the higher capacitive current attainable by the BP electrode.

densities for the negative and positive electrolytes were higher for the BP electrode than those for the CP electrode, reflecting the greater electrochemical conversion of the active species on its surface. To investigate the reason for the higher current densities obtained with the BP electrode, we performed double-layer capacitance measurements to determine surface area utilization. Cyclic voltammograms were acquired for each of the electrodes in a blank solution of 0.05 M $TEABF_4$ in acetonitrile (Fig. 6c) over a narrow range of voltages to eliminate faradaic currents. A plot of double-layer current versus scan rate was linear (not shown), indicating the capacitive behavior in the scanned potential range. The slope of the fitted line was used to estimate the double-layer capacitance (C_{DL}) of the system according to Equation 3, which was then used, along with the assumed area specific reference capacitance, to obtain the electrochemically active surface area (ECSA) by means of Equation 4, as described in the literature:[65,66]

$$i_{DL} = vC_{DL} \quad [3]$$

$$\text{ECSA} = C_{DL}/C_s \quad [4]$$

where i_{DL} is double-layer current, v is scan rate, and C_s is the assumed area specific reference capacitance for the electrode material. The area specific capacitance of an alumina-polished smooth GCE with a known surface area, was measured in a solution of 0.05 M $TEABF_4$ in acetonitrile, and was determined to be equal to 12 μF cm^{-2}. This value was assumed to be equal to the C_s value for both BP and the CP electrodes in the same experimental conditions. A similar approach was performed by Sun et al.[67] As can be seen in Table III, the ECSA of the BP electrode was ≈193 times that of the CP, indicating that the number of sites available for an electrochemical reaction on the former was much larger than that of the latter. Surface area utilization can be evaluated from the ratio of the ECSA to the BETSA, a ratio that is also an indicator of the wettability of the electrode. Calculation of this ratio indicated that ≈19% of the BETSA of the BP electrode was utilized, compared with only ≈10% for the CP electrode; leading to the higher current density obtained with the former electrode.

Table III. Comparison of surface area utilization by the BP and CP electrodes.[a]

Parameter	BP	CP
ρ (g cm^{-2})	0.00346	0.00850
ECSA (m^2 g^{-1})	36.644	0.185
ECSA:BETSA (%)	19.29	10.28

[a]ρ = material density; ECSA = electrochemically active surface area; BETSA = total surface area as measured by BET analysis. ECSA/BETSA ratio is indicative of electrode wettability.

To further evaluate the electrochemical behavior of the electrodes, we used the voltammograms shown in Fig. 4 insets. Over different v, the ratio of anodic peak current to cathodic peak current (I_{pa}/I_{pc}) in Figs. 7c, 7d deviated slightly from unity indicating possible coupled non-electrochemical reactions (usually irreversible chemical decompositions) that accompany the electrochemistry. On the electrochemical reversibility, the peak potential separation (ΔE_p) ranged from 87 to 131 mV for the CP electrode and from 212 to 438 mV for the BP electrode in the negative electrolyte (Fig. 7a), and from 64 to 90 mV for the CP electrode and from 101 to 203 mV for the BP electrode in the positive electrolyte (Fig. 7b), confirming the electrochemical irreversibility of the redox reactions at these electrodes.

Because the reactions on both the CP and the BP electrodes meet the quasi-reversibility criteria[63] (Fig. 4 insets, Fig. 7), we used a combination of Nicholson's method[68,69] and Klingler and Kochi method[70] to calculate the heterogeneous rate constant (k^o) of the redox reactions at the electrodes. Lavagnini et al.[71] gave empirical equations that can be used to combine both methods for evaluating k^o as shown below (for a single electron transfer):

$$\psi = \frac{-0.6288 + 0.0021\Delta E_p}{1 - 0.017\Delta E_p} \quad [5]$$

$$\psi = 2.18\left(\frac{\alpha}{\pi}\right)^{\frac{1}{2}} \exp\left(\frac{-\alpha^2 F}{RT}\Delta E_p\right) \quad [6]$$

with

$$\psi = k^o\left(\frac{\pi D v F}{RT}\right)^{-\frac{1}{2}} \quad [7]$$

where F is Faraday's constant, α is transfer coefficient, D is the diffusion coefficient of the active species, R is the gas constant and T is temperature. A plot of ψ vs. $(\frac{\pi DF}{RT})^{-\frac{1}{2}} v^{-\frac{1}{2}}$ gives a slope equals to k^o. Eq. 5 is valid for ΔE_p in the range between 61 and 212 mV, whereas Eq. 6 is applicable for 212 mV > ΔE_p. These equations were applied assuming $\alpha = 0.5$ and $D = 3.93 \times 10^{-6}$ cm^2 s^{-1}.[48]

For both positive and negative redox couples' reactions, the values of k^o obtained with the CP electrode were much greater than

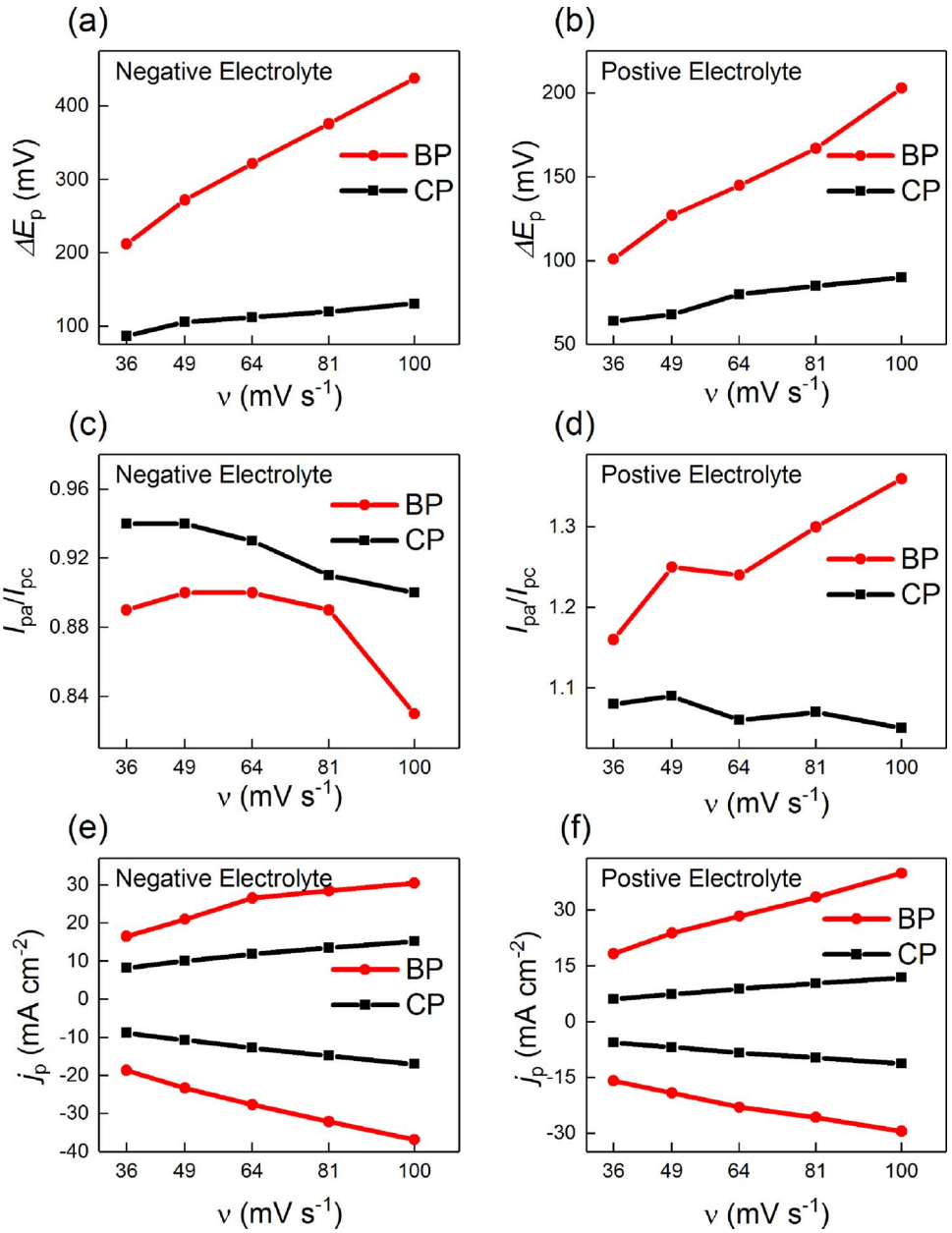

Figure 7. Analysis of iR-corrected cyclic voltammograms for BP and CP electrodes in an acetonitrile solution of $V(acac)_3$ (0.01 M) and $TEABF_4$ (0.05 M) at room temperature scanned for the negative and positive redox couples showing (a,b) plots of peak separations versus scan rate, (c,d) plots of peak ratios versus scan rate, and (e,f) plots of peak currents versus scan rate. The plots show the irreversibility of the electrodes, and suggest that the electrodes meet the quasi-reversibility criterion.

those obtained with the BP electrode (Table IV), indicating the higher activity of the CP electrode toward the $[V(acac)_3]^+/[V(acac)_3]^0$ and $[V(acac)_3]^-/[V(acac)_3]^0$ redox couples. Even though higher current densities were obtained with the BP electrode due to better surface area utilization in comparison to the CP electrode, the BP electrode has less efficient kinetic facility for the investigated redox couples. We attribute the slower kinetics at the BP electrode to the possibility that the available sites for the reaction were dominated by the basal sites of the MWCNTs; researchers have shown that basal sites exhibit lower electrochemical activity in contrast to edge sites.[72]

Table IV. Performance indexes for the CP and BP electrodes calculated for the positive redox couple, $[V(acac)_3]^0/[V(acac)_3]^+$), and the negative redox couple, $[V(acac)_3]^0/[V(acac)_3]^-$).[a]

Electrode	Redox couple	$k^o \times 10^{-3}$ (cm s^{-1})
CP	Positive	48.68
	Negative	6.27
BP	Positive	4.99
	Negative	0.69

[a] k^o = standard heterogeneous rate constant.

Electrochemical impedance spectroscopy.—We used electrochemical impedance spectroscopy (EIS) to investigate the kinetics of the CP and BP electrodes for the $[V(acac)_3]^0/[V(acac)_3]^-$ and $[V(acac)_3]^0/[V(acac)_3]^+$ redox couples in an acetonitrile solution of 0.01 M $V(acac)_3$ and 0.05 M $TEABF_4$ (Fig. 8). This was done by performing EIS at equilibrium potentials of the $[V(acac)_3]^0/[V(acac)_3]^-$ and $[V(acac)_3]^0/[V(acac)_3]^+$ redox couples (−1.8 and 0.4 V

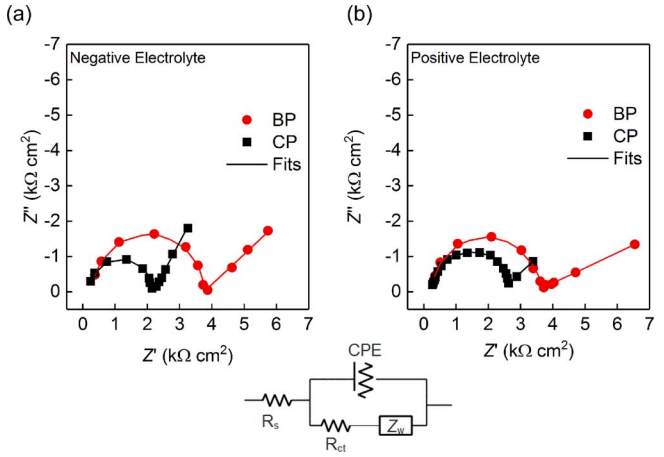

Figure 8. Electrochemical impedance spectra for BP and CP electrodes in an acetonitrile solution of $V(acac)_3$ (0.01 M) and TEABF4 (0.05 M) at room temperature performed at the equilibrium potentials of the (a) negative and (b) positive redox couples. Data was fitted using a Randles equivalent circuit shown in the inset; where R_s is the solution resistance, R_{ct} is the charge transfer resistance, CPE is a constant phase element and Z_w is a warburg impedance term.

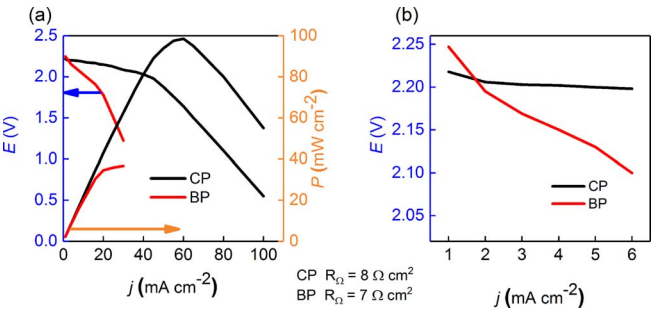

Figure 9. (a) Plots of iR-corrected polarization curves showing the variation of potential versus current density and the variation of power density versus current density for the BP and CP electrodes for the full range of current densities, and (b) plots of iR-corrected polarization curves at low current density range for clarity. The compensated area-specific-iR losses (R_Ω) are given in the insets for both electrodes. The plots resemble the higher power density, lower activation over potential and better mass transport facilitation attainable by the CP electrode as compared with the BP electrode.

respectively). Nyquist plots of both electrodes resembled a depressed semi-circle at the high frequency region and a sloped line at the low frequency region ascribed to charge transfer process and the Warburg diffusion process respectively. The EIS data were fitted using a Randles equivalent circuit (Fig. 8 inset) which utilized a constant phase element (CPE) instead of a pure capacitance element to attain a more accurate fit of the experimental data, and we obtained the charge transfer resistance (R_{ct}), the double layer capacitance (C_{dl}), and the Warburg impedance (Z_w) values to improve our understanding of the electrode's kinetics and to supplement our CV studies, as given in Table V.

R_{ct} for the CP electrode was consistently lower for both the negative and the positive redox couples indicating the higher activity of the CP electrode as compared to the BP electrode, and providing further support to our cyclic voltammetry analysis. On the other hand, C_{dl} was consistently higher for the CP electrode, indicating that the amount of active sites available for a reaction is higher for the CP as compared with the BP. Interestingly, these results come in contrast with our capacitance analysis which showed a higher ECSA and surface utilization of the BP electrode (as described in Cyclic voltammetry section). We attribute the lower C_{dl} values that were demonstrated by the BP electrode during the EIS measurements (in presence of the active species) to the higher limitation of mass transport and diffusion of active species in the electrolyte within the pores of the BP, as compared with the CP electrode. Z_w values, related to the diffusion processes of the active species, for the CP electrode were consistently lower than that for the BP electrodes, and were ascribed to the lower concentration over potential of the ion diffusion processes which may have been facilitated by the markedly lower effects of the thin layer diffusion within the pores of the CP electrode as compared to that of the BP electrode (as described in Cyclic voltammetry section).

Table V. Charge transfer resistance (R_{ct}), double layer capacitance (C_{dl}), and warburg impedance (Z_w) values obtained by fitting the electrochemical impedance spectra for the positive redox couple, $[V(acac)_3]^0/[V(acac)_3]^+$), and the negative redox couple, $[V(acac)_3]^0/[V(acac)_3]^-$).

Electrode	Redox couple	R_{ct} (Ω cm^2)	C_{dl} (μF cm^{-2})	Z_w (Ω cm^2)
CP	Positive	2551	0.0368	4.8×10^{-13}
	Negative	2016	0.0506	1.5×10^{-12}
BP	Positive	3199	0.0341	1.6×10^{-5}
	Negative	3506	0.0317	2.5×10^{-6}

Polarization curve.—In order to understand the different roles played by each of the electrode's kinetics and internal structures in their overall performance when employed in a flow cell, we performed iR-corrected discharge polarization curves (as described in literature[73]) at a constant state of charge (SOC = 50%) for flow cells incorporating the CP and BP electrodes, to investigate losses associated with activation, ohmic, and concentration over potentials. Two types of ohmic losses can occur in our flow cell setup; which are iR losses that can be measured by EIS at the high frequency region and are related to ionic and contact resistances, and pseudo-iR losses which do not contribute to the iR measurements by EIS at high frequency region and are related to mass transport within the electrodes.[74] Thus, the iR-corrected polarization curves (which were compensated by the EIS measurements at high frequency regions) shown in Fig. 9, have the advantage of being free from contact and ionic iR losses, while retaining the pseudo-iR losses related to the thin layer diffusion within the pores of the CP and BP electrodes. As illustrated (Fig. 9), the limiting current density was 100 and 30 mA cm^{-2}, and the peak power density was 98 and 37 mW cm^{-2} for the flow cells incorporating the CP and the BP electrodes respectively, indicating a 3-fold increase in the performance of the flow cell incorporating the CP electrode as compared to that incorporating the BP electrode.

Activation over potential losses become significant at low current densities, at which the flow cell's performance becomes limited by the activity of the electrodes. We have already established that the electrochemical activity of CP is larger than that of the BP electrode (as described in Cyclic voltammetry sections and Electrochemical impedance spectroscopy), and as expected, the drop in voltage losses due to the electrodes' activation over potentials was larger for the BP electrode (120 mV) as compared to the CP electrode (15 mV).

Pseudo-iR losses due to the thin layer diffusion within the electrodes are directly related to the linear slope of the ohmic region in the iR-corrected polarization curves. We have already demonstrated that the effect of thin layer diffusion within the BP electrode is higher than that in the CP electrode (as described in Cyclic voltammetry section), and as expected, the area specific pseudo resistance was 4.2 times larger at the BP electrode (20.22 Ω cm^2) than that at the CP electrode (4.72 Ω cm^2), indicating that mass transport of active species within the active layers of the CP electrode was markedly better than that of the BP electrode.

Finally, losses due to concentration and transport of the bulk electrolyte to the active sites are related to the final drop region in the polarization curve, and with this regards, the flow cell utilizing the CP electrodes was superior to that utilizing the BP electrodes, suggesting

that the BP electrodes significantly impeded the flow of the electrolyte within the flow fields as compared with that by the CP electrodes. At high current densities (>30 mA cm^{-2}), the rate of electrochemical conversion at the active sites becomes sufficiently large that mass transport is insufficient to replenish active species consumed at those sites. On the other hand, the flow cell utilizing the CP electrodes sustained a markedly higher limiting current density (100 mA cm^{-2}).

Charge–discharge cycling.—We performed charge–discharge cycling tests using a single layer of each of the CP and the BP electrodes in the positive and the negative half-cells. We initially attempted charge-discharge experiments (not shown) using low electrolyte concentrations (0.01 M $V(acac)_3$ and 0.05 M $TEABF_4$) with a TEA^+ conducting Nafion membrane, but very low coulombic and resulting energy efficiencies values were recorded (due to high electrolyte/cell internal resistance). In addition, long charge-discharge cycling tests were not achievable due to the high crossover resulting in severe capacity decay. Therefore, we improved the experimental setup by utilizing an electrolyte of 0.05 M $V(acac)_3$ and 0.2 M $TEABF_4$ in acetonitrile, and the low permeability NafionSi membrane.[44] Cycling was conducted at a constant current density of 50 and 25 mA cm^{-2} for the flow cells incorporating the CP and BP electrodes respectively, and the calculated efficiencies (η) as a function of cycle number are shown in Fig. 10. We have already established that the BP electrode exhibited a higher electrical conductivity (by a factor of ≈1.77) and a larger ECSA (by a factor of ≈193) than the CP electrodes, whereas the CP electrode exhibited a higher heterogeneous rate constant (by a factor >9). Nevertheless, the coulombic efficiencies (CE) for both electrodes became more stable after the twentieth cycle and averaged higher for the CP electrode (100%) than for the BP electrode (93%). The high columbic efficiencies were attainable due to the use of the NafionSi membranes and a reasonable molarity of electrolytes in the flow cell setups. On the other hand, the voltage efficiencies (VE) average at 90% for the CP electrode and 88% for the BP electrode, which can be attributed to the higher activity and lower ohmic resistance of the CP electrode. The obtained trends in VE were attributed to the combined

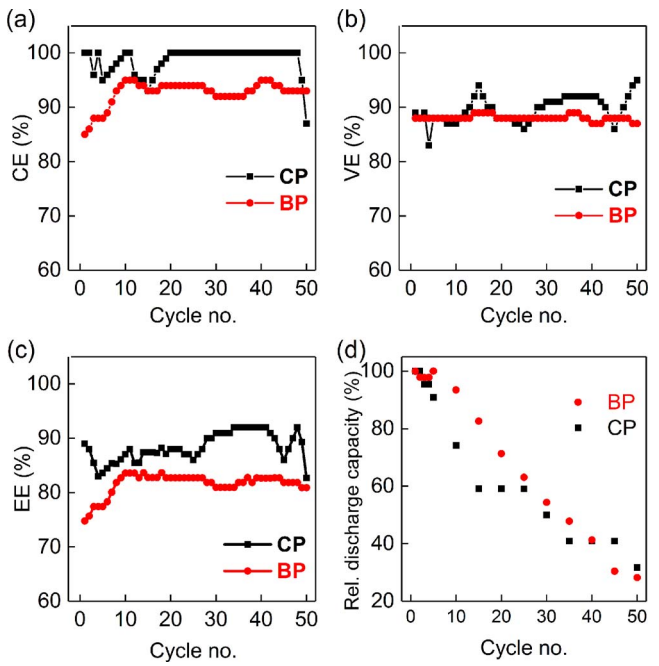

Figure 10. Charge discharge analysis for 50 cycles utilizing a flow cell with an electrolyte comprising of 0.05 M $V(acac)_3$ and 0.2 M $TEABF_4$ in acetonitrile showing the (a) CE, (b) VE, (c) EE, and (d) relative discharge capacity versus cycle number for the BP and CP electrodes. The CP electrode resembled a higher EE and a lower relative discharge capacity over cycling as compared with the BP electrode.

effects of species crossover and the different flow regimes in the two electrodes (due to their structural differences, as described in section Morphological and physical characterization of the electrodes). The good performance of both electrodes, however, compares reasonably well to recently reported efficiencies utilizing similar setups, membranes (NafionSi) and electrolyte concentrations.[44] Even though the CP electrode resembled a significantly larger ko as compared with the BP electrode, the VE for both electrodes were not largely different, which can be attributed to the role of the high-BET-surface-area of the BP electrode. The effects of the higher surface area but lower activity of the BP electrode as compared with the lower surface area but higher activity of the CP electrode (as described in Cyclic voltammetry section), together with their different flow regimes, gave rise to their respective cycling efficiencies. The fluctuations in efficiencies seen during long charge-discharge cycling can be ascribed to flow inconsistencies (usually observed when a serpentine flow field is used in a relatively small area cell). In addition, electrolyte membrane interaction/ degradation,[44] and effects of agglomeration (as described in Microscopy section) can also contribute to the fluctuations recorded. In order to improve the VE at the BP electrode, we suggest investigating the use of catalysts within the MWCNTs fibers to increase their activity toward the redox couple. On the other hand, in order to improve the VE at the CP electrode, we suggest investigating the use of various treatments to modify the surface chemistries and thus improve the currently low ECSA:BETSA ratio (as given in Table III).

The energy efficiencies (EE = CE × VE) averaged 89% for the CP electrode and 82% for the BP electrode throughout the cycling test. These excellent EE values were due to the excellent electrochemical activity of the CP and the high ECSA of the BP.

Moreover, relative discharge capacity versus cycle number (Fig. 10d) was plotted to visualize the capability of the flow cells incorporating the porous carbon electrodes in retaining discharge capacity over cycling. Capacity decay occurred gradually and consistently for both flow cells and the relative discharge capacities per cycle were consistently higher when the BP electrode was employed until the 40th cycle, after which the CP retained higher relative discharge capacities. Interestingly, the rate of relative discharge capacity was constant for the cell employing the BP electrode, and was variant for the cell incorporating the CP electrode. These results can be related to the stable VE for the cell incorporating the BP electrode, and the relatively inconsistent VE values for the cell incorporating the CP electrode, and can suggest that the relative discharge capacity can be favored by a lower VE, possibly due to the relatively decreased participation of active specie in their electrochemical conversion at the electrode's interface, and therefore limiting capacity decay.

Conclusions

A commercially available CP electrode and an in-lab fabricated BP electrode (a freestanding sheet of MWCNTs) were investigated as both the positive and the negative electrodes for non-aqueous VRFBs. Being investigated in their freestanding forms, no metal substrates were involved, eliminating the effects of mixed kinetics, and thus, permitting the measurement of their true electrochemical response. The CP electrode demonstrated heterogeneous rate constants of 4.8 × 10^{-2} and 3.9 × 10^{-6} cm s^{-1} for the positive and the negative electrolytes respectively, both of which were more than 9 times faster than that obtained by the BP electrode, reflecting the higher reversibility of the CP electrode toward both positive and negative redox couples. Moreover, the effect of thin layer diffusion within the porous structure of BP electrode is markedly higher than the CP electrode as shown by our voltammetry analysis, giving rise to different flow regimes. Thus, engineering the porous structure of these electrodes is needed. Flow cells performance experiments revealed that the CP electrode was superior in facilitating a higher power density (98 mW cm^{-2}), limiting current density (100 mA cm^{-2}), and energy efficiency (89%) as compared to the BP electrode (37 mW cm^{-2}, 30 mA cm^{-2}, and 82% respectively), which were attributed to the combined effects of the higher surface area but lower activity of the BP electrode as compared with the lower

surface area but higher activity of the CP electrode, together with their different flow regime. Polarization curve analysis revealed that activation, ohmic, and concentration losses were consistently lower for the cell employing the CP electrode. Charge–discharge cycling demonstrated the effects of the respective electrode properties toward the exhibited cycling efficiencies, suggesting that various treatments and/or modifications can be prescribed in order to obtain improved performances. These results provide interesting insights into the electrochemical activity of different carbon-based porous electrodes for non-aqueous VRFBs, whilst highlighting the potential of MWCNTs in the form of freestanding sheets, for the application of electrodes in NARFBs.

Acknowledgments

This work was funded by the Cooperative Agreement between the Masdar Institute of Science and Technology (Masdar Institute), Abu Dhabi, UAE and the Massachusetts Institute of Technology (MIT), Cambridge, MA, USA - Reference 02/MI/MI/CP/11/07633/GEN/G/00. The authors acknowledge the support of Applied NanoStructured Solutions LLC, a Lockheed Martin Company, for providing the carbon nanostructured flakes.

References

1. U. S. Energy Information Administration (EIA), International Energy Outlook 2016 (IEO 2016), (2016).
2. M. O. Bamgbopa, S. Almheiri, and H. Sun, Prospects of recently developed membraneless cell designs for redox flow batteries, *Renew. Sustain. Energy Rev.*, **70**, 506 (2017).
3. Thaller and H. Lawrence, *Energy storage system.*, 3,996,064, n.d.
4. A. Z. Weber, M. M. Mench, J. P. Meyers, P. N. Ross, J. T. Gostick, and Q. Liu, Redox flow batteries: a review, *J. Appl. Electrochem.*, **41**, 1137 (2011).
5. M. Skyllas-Kazacos, M. H. Chakrabarti, S. A. Hajimolana, F. S. Mjalli, and M. Saleem, Progress in Flow Battery Research and Development, *J. Electrochem. Soc.*, **158**, R55 (2011).
6. M. Rychcik and M. Skyllas-Kazacos, Characteristics of a new all-vanadium redox flow battery, *J. Power Sources*, **22**, 59 (1988).
7. H. S. Lim, A. M. Lackner, and R. C. Knechtli, Zinc-Bromine Secondary Battery, *J. Electrochem. Soc.*, **124**, 1154 (1977).
8. W. Wang, S. Kim, B. Chen, Z. Nie, J. Zhang, G.-G. Xia, L. Li, and Z. Yang, A new redox flow battery using Fe/V redox couples in chloride supporting electrolyte, *Energy Environ. Sci.*, **4**, 4068 (2011).
9. P. K. Leung, C. Ponce-de-León, C. T. J. Low, A. A. Shah, and F. C. Walsh, Characterization of a zinc–cerium flow battery, *J. Power Sources*, **196**, 5174 (2011).
10. Q. Liu, A. E. Sleightholme, A. A. Shinkle, Y. Li, and L. T. Thompson, Non-aqueous vanadium acetylacetonate electrolyte for redox flow batteries, *Electrochem. Commun.*, **11**, 2312 (2009).
11. Q. Liu, A. A. Shinkle, Y. Li, C. W. Monroe, L. T. Thompson, and A. E. Sleightholme, Non-aqueous chromium acetylacetonate electrolyte for redox flow batteries, *Electrochem. Commun.*, **12**, 1634 (2010).
12. A. E. Sleightholme, A. A. Shinkle, Q. Liu, Y. Li, C. W. Monroe, and L. T. Thompson, Non-aqueous manganese acetylacetonate electrolyte for redox flow batteries, *J. Power Sources*, **196**, 5742 (2011).
13. Y. Matsuda, K. Tanaka, M. Okada, Y. Takasu, M. Morita, and T. Matsumura-Inoue, A rechargeable redox battery utilizing ruthenium complexes with non-aqueous organic electrolyte, *J. Appl. Electrochem.*, **18**, 909 (1988).
14. M.-S. Park, N.-J. Lee, S.-W. Lee, K. J. Kim, D.-J. Oh, and Y.-J. Kim, High-Energy Redox-Flow Batteries with Hybrid Metal Foam Electrodes, *ACS Appl. Mater. Interfaces.*, **6**, 10729 (2014).
15. J. Mun, M.-J. Lee, J.-W. Park, D.-J. Oh, D.-Y. Lee, and S.-G. Doo, Non-aqueous redox flow batteries with nickel and iron tris (2, 2′-bipyridine) complex electrolyte, *Electrochem. Solid-State Lett.*, **15**, A80 (2012).
16. F. R. Brushett, J. T. Vaughey, and A. N. Jansen, An All-Organic Non-aqueous Lithium-Ion Redox Flow Battery, *Adv. Energy Mater.*, **2**, 1390 (2012).
17. M. Duduta, B. Ho, V. C. Wood, P. Limthongkul, V. E. Brunini, W. C. Carter, and Y.-M. Chiang, Semi-Solid Lithium Rechargeable Flow Battery, *Adv. Energy Mater.*, **1**, 511 (2011).
18. Z. Li, K. C. Smith, Y. Dong, N. Baram, F. Y. Fan, J. Xie, P. Limthongkul, W. C. Carter, and Y.-M. Chiang, Aqueous semi-solid flow cell: demonstration and analysis, *Phys. Chem. Chem. Phys.*, **15**, 15833 (2013).
19. F. Y. Fan, W. H. Woodford, Z. Li, N. Baram, K. C. Smith, A. Helal, G. H. McKinley, W. C. Carter, and Y.-M. Chiang, Polysulfide Flow Batteries Enabled by Percolating Nanoscale Conductor Networks, *Nano Lett.*, **14**, 2210 (2014).
20. S. Hamelet, D. Larcher, L. DuPont, and J.-M. Tarascon, Silicon-Based Non Aqueous Anolyte for Li Redox-Flow Batteries, *J. Electrochem. Soc.*, **160**, A516 (2013).
21. H. Chen, Q. Zou, Z. Liang, H. Liu, Q. Li, and Y.-C. Lu, Sulphur-impregnated flow cathode to enable high-energy-density lithium flow batteries, *Nat. Commun.*, **6**, 5877 (2015).
22. E. Ventosa, D. Buchholz, S. Klink, C. Flox, L. G. Chagas, C. Vaalma, W. Schuhmann, S. Passerini, and J. R. Morante, Non-aqueous semi-solid flow battery based on Na-ion chemistry. P2-type $Na_xNi_{0.22}Co_{0.11}Mn_{0.66}O_2$–$NaTi_2(PO_4)_3$, *Chem. Commun.*, **51**, 7298 (2015).
23. T. Janoschka, N. Martin, U. Martin, C. Friebe, S. Morgenstern, H. Hiller, and M. D. Hager, U. S. Schubert, An aqueous, polymer-based redox-flow battery using non-corrosive, safe, and low-cost materials, *Nature*, **527**, 78 (2015).
24. H. Chen and Y.-C. Lu, A High-Energy-Density Multiple Redox Semi-Solid-Liquid Flow Battery, *Adv. Energy Mater.*, **6**, n/a-n/a (2016).
25. F. Soavi, I. Ruggeri, and C. Arbizzani, A Novel, Semi-Solid Li/O_2 Redox Flow Battery, *Meet. Abstr.*, **MA2016-01**, 234 (2016).
26. S.-H. Shin, S.-H. Yun, and S.-H. Moon, A review of current developments in non-aqueous redox flow batteries: characterization of their membranes for design perspective, *Rsc Adv.*, **3**, 9095 (2013).
27. A. Parasuraman, T. M. Lim, C. Menictas, and M. Skyllas-Kazacos, Review of material research and development for vanadium redox flow battery applications, *Electrochimica Acta*, **101**, 27 (2013).
28. W. Wang, Q. Luo, B. Li, X. Wei, L. Li, and Z. Yang, Recent Progress in Redox Flow Battery Research and Development, *Adv. Funct. Mater.*, **23**, 970 (2013).
29. K. J. Kim, M.-S. Park, Y.-J. Kim, J. H. Kim, S. X. Dou, and M. Skyllas-Kazacos, A technology review of electrodes and reaction mechanisms in vanadium redox flow batteries, *J. Mater. Chem. A*, **3**, 16913 (2015).
30. F. Pan and Q. Wang, Redox Species of Redox Flow Batteries: A Review, *Mol. Basel Switz.*, **20**, 20499 (2015).
31. Chapter on "*Secondary Batteries: Redox Flow Battery—Vanadium Redox*," *by Maria Skyllas-Kazacos Encyclopedia of Electrochemical Power Sources*, J. Garche, P. Moseley, Z. Ogumi, D. Rand, and B. Scrosati, Editors, Elsevier, New York, USA, pp. 444, 2009., in: n.d.
32. M. Skyllas-Kazacos, M. Rychcik, R. G. Robins, A. G. Fane, and M. A. Green, New All-Vanadium Redox Flow Cell, *J. Electrochem. Soc.*, **133**, 1057 (1986).
33. M. Skyllas-Kazacos, G. Kazacos, G. Poon, and H. Verseema, Recent advances with UNSW vanadium-based redox flow batteries, *Int. J. Energy Res.*, **34**, 182 (2010).
34. L. Li, S. Kim, W. Wang, M. Vijayakumar, Z. Nie, B. Chen, J. Zhang, G. Xia, J. Hu, G. Graff, J. Liu, and Z. Yang, A Stable Vanadium Redox-Flow Battery with High Energy Density for Large-Scale Energy Storage, *Adv. Energy Mater.*, **1**, 394 (2011).
35. M. L. Perry, R. M. Darling, and R. Zaffou, High Power Density Redox Flow Battery Cells, *ECS Trans.*, **53**, 7 (2013).
36. M. Ulaganathan, V. Aravindan, Q. Yan, S. Madhavi, M. Skyllas-Kazacos, and T. M. Lim, Recent Advancements in All-Vanadium Redox Flow Batteries, *Adv. Mater. Interfaces.*, **3**, n/a-n/a (2016).
37. A. Lucas and S. Chondrogiannis, Smart grid energy storage controller for frequency regulation and peak shaving, using a vanadium redox flow battery, *Int. J. Electr. Power Energy Syst.*, **80**, 26 (2016).
38. C.-N. Sun, M. M. Mench, and T. A. Zawodzinski, High Performance Redox Flow Batteries: An Analysis of the Upper Performance Limits of Flow Batteries Using Non-aqueous Solvents, *Electrochimica Acta.*, (n.d.).
39. B. Li, M. Gu, Z. Nie, Y. Shao, Q. Luo, X. Wei, X. Li, J. Xiao, C. Wang, V. Sprenkle, and W. Wang, Bismuth Nanoparticle Decorating Graphite Felt as a High-Performance Electrode for an All-Vanadium Redox Flow Battery, *Nano Lett.*, **13**, 1330 (2013).
40. X. Wu, H. Xu, L. Lu, H. Zhao, J. Fu, Y. Shen, P. Xu, and Y. Dong, PbO_2-modified graphite felt as the positive electrode for an all-vanadium redox flow battery, *J. Power Sources*, **250**, 274 (2014).
41. X. L. Zhou, T. S. Zhao, L. An, Y. K. Zeng, and X. B. Zhu, Performance of a vanadium redox flow battery with a VANADion membrane, *Appl. Energy.*, **180**, 353 (2016).
42. B. Jiang, L. Wu, L. Yu, X. Qiu, and J. Xi, A comparative study of Nafion series membranes for vanadium redox flow batteries, *J. Membr. Sci.*, **510**, 18 (2016).
43. M. O. Bamgbopa, N. Pour, Y. Shao-Horn, and S. Almheiri, Systematic selection of solvent mixtures for non-aqueous redox flow batteries – vanadium acetylacetonate as a model system, *Electrochimica Acta*, **223**, 115 (2017).
44. M. O. Bamgbopa and S. Almheiri, Influence of solvents on species crossover and capacity decay in non-aqueous vanadium redox flow batteries: Characterization of acetonitrile and 1, 3 dioxolane solvent mixture, *J. Power Sources*, **342**, 371 (2017).
45. S.-H. Shin, Y. Kim, S.-H. Yun, S. Maurya, and S.-H. Moon, Influence of membrane structure on the operating current densities of non-aqueous redox flow batteries: Organic–inorganic composite membranes based on a semi-interpenetrating polymer network, *J. Power Sources*, **296**, 245 (2015).
46. P. S. Son, M.-S. Oh, J.-H. Ye, and S.-H. Choi, Counter anion effects in anion exchange membrane-fabricated non-aqueous vanadium redox flow battery, *Anal. Sci. Technol.*, **28**, 341 (2015).
47. K.-W. Sung, S.-H. Shin, and S.-H. Moon, Characterization of Commercial Membranes for Non-aqueous Vanadium Redox Flow Battery, *Korean Chem. Eng. Res.*, **51**, 615 (2013).
48. A. A. Shinkle, A. E. Sleightholme, L. T. Thompson, and C. W. Monroe, Electrode kinetics in non-aqueous vanadium acetylacetonate redox flow batteries, *J. Appl. Electrochem.*, **41**, 1191 (2011).
49. D. Zhang, Q. Liu, X. Shi, and Y. Li, Tetrabutylammonium hexafluorophosphate and 1-ethyl-3-methyl imidazolium hexafluorophosphate ionic liquids as supporting electrolytes for non-aqueous vanadium redox flow batteries, *J. Power Sources*, **203**, 201 (2012).
50. J. Lee, M.-S. Park, and K. J. Kim, Highly enhanced electrochemical activity of Ni foam electrodes decorated with nitrogen-doped carbon nanotubes for non-aqueous redox flow batteries, *J. Power Sources*, **341**, 212 (2017).
51. S. A. Sharief, R. A. Susantyoko, M. Alhashem, and S. Almheiri, Synthesis of few-layer graphene-like sheets from carbon-based powders via electrochemical exfoliation, using carbon black as an example, *J. Mater. Sci.*, **52**, 11004 (2017).

52. *3D Graphene–Ni Foam as an Advanced Electrode for High-Performance Nonaqueous Redox Flow Batteries - ACS Applied Materials & Interfaces (ACS Publications)*, (n.d.). http://pubs.acs.org/doi/abs/10.1021/acsami.7b04777 (accessed August 7, 2017).
53. M. O. Bamgbopa, Y. Shao-Horn, and S. Almheiri, The potential of non-aqueous redox flow batteries as fast-charging capable energy storage solutions: demonstration with an iron–chromium acetylacetonate chemistry, *J. Mater. Chem. A*, **5**, 13457 (2017).
54. F. Khan, A. Kausar, and M. Siddiq, A Review on Properties and Fabrication Techniques of Polymer/Carbon Nanotube Composites and Polymer Intercalated Buckypapers, *Polym.-Plast. Technol. Eng.*, **54**, 1524 (2015).
55. I. Mustafa, I. Lopez, H. Younes, R. A. Susantyoko, R. A. Al-Rub, and S. Almheiri, Fabrication of Freestanding Sheets of Multiwalled Carbon Nanotubes (Buckypapers) for Vanadium Redox Flow Batteries and Effects of Fabrication Variables on Electrochemical Performance, *Electrochimica Acta*, **230**, 222 (2017).
56. M. F. Arif, S. Kumar, and T. Shah, Tunable morphology and its influence on electrical, thermal and mechanical properties of carbon nanostructure-buckypaper, *Mater. Des.*, **101**, 236 (2016).
57. T. K. Shah, H. C. Malecki, R. R. Basantkumar, H. Liu, C. A. FLEISCHER, J. J. Sedlak, J. M. Patel, W. P. BURGESS, and J. M. Goldfinger, Carbon nanostructures and methods of making the same, US20140093728 A1, 2014. http://www.google.com/patents/US20140093728 (accessed August 6, 2016).
58. J. Xi, Z. Wu, X. Qiu, and L. Chen, Nafion/SiO_2 hybrid membrane for vanadium redox flow battery, *J. Power Sources*, **166**, 531 (2007).
59. J. K. Park, J. Spano, R. B. Moore, and S. Wi, Counterion motions and thermal ordering effects in perfluorosulfonate ionomers probed by solid-state NMR, *Polymer*, **50**, 5720 (2009).
60. I. Streeter, G. G. Wildgoose, L. Shao, and R. G. Compton, Cyclic voltammetry on electrode surfaces covered with porous layers: An analysis of electron transfer kinetics at single-walled carbon nanotube modified electrodes, *Sens. Actuators B Chem.*, **133**, 462 (2008).
61. E. Lust, G. Nurk, A. Jänes, M. Arulepp, L. Permann, P. Nigu, and P. Möller, Electrochemical properties of nanoporous carbon electrodes, *Condens Matter Phys.*, **5**, 307 (2002).
62. K. M. Kadish, J. Q. Ding, and T. Malinski, Resistance of nonaqueous solvent systems containing tetraalkylammonium salts. Evaluation of heterogeneous electron transfer rate constants for the ferrocene/ferrocenium couple, *Anal. Chem.*, **56**, 1741 (1984).
63. Wiley: *Electrochemical Methods: Fundamentals and Applications*, 2nd Edition - Allen J. Bard and Larry R. Faulkner, (n.d.). http://eu.wiley.com/WileyCDA/WileyTitle/productCd-0471043729.html (accessed October 3, 2016).
64. K. Izutsu, Potentiometry in Non-Aqueous Solutions, in: Electrochem. Nonaqueous Solut., *Wiley-VCH Verlag GmbH & Co. KGaA*, 167 (2002).
65. B. V. Tilak, C. G. Rader, and S. K. Rangarajan, Techniques for Characterizing Porous Electrodes I: Determination of the Double Layer Capacity, *J. Electrochem. Soc.*, **124**, 1879 (1977).
66. S. Trasatti and O. A. Petrii, Real surface area measurements in electrochemistry, *J. Electroanal. Chem.*, **327**, 353 (1992).
67. C.-N. Sun, F. M. Delnick, L. Baggetto, G. M. Veith, and T. A. Zawodzinski, Hydrogen evolution at the negative electrode of the all-vanadium redox flow batteries, *J. Power Sources*, **248**, 560 (2014).
68. R. S. Nicholson and I. Shain, Theory of Stationary Electrode Polarography. Single Scan and Cyclic Methods Applied to Reversible, Irreversible, and Kinetic Systems., *Anal. Chem.*, **36**, 706 (1964).
69. R. S. Nicholson, Theory and Application of Cyclic Voltammetry for Measurement of Electrode Reaction Kinetics., *Anal. Chem.*, **37**, 1351 (1965).
70. R. J. Klingler and J. K. Kochi, Electron-transfer kinetics from cyclic voltammetry. Quantitative description of electrochemical reversibility, *J. Phys. Chem.*, **85**, 1731 (1981).
71. I. Lavagnini, R. Antiochia, and F. Magno, An Extended Method for the Practical Evaluation of the Standard Rate Constant from Cyclic Voltammetric Data, *Electroanalysis*, **16**, 505 (2004).
72. N. Pour, D. G. Kwabi, T. Carney, R. M. Darling, M. L. Perry, and Y. Shao-Horn, Influence of Edge- and Basal-Plane Sites on the Vanadium Redox Kinetics for Flow Batteries, *J. Phys. Chem. C*, **119**, 5311 (2015).
73. A. W. Burch, Characterization Techniques and Electrolyte Separator Performance Investigation for All Vanadium Redox Flow Battery, University of Tennessee, 2015.
74. D. Aaron, Z. Tang, A. B. Papandrew, and T. A. Zawodzinski, Polarization curve analysis of all-vanadium redox flow batteries, *J. Appl. Electrochem.*, **41**, 1175 (2011).
75. A. A. Shinkle, A. E. Sleightholme, L. D. Griffith, L. T. Thompson, and C. W. Monroe, Degradation mechanisms in the non-aqueous vanadium acetylacetonate redox flow battery, *J. Power Sources*, **206**, 490 (2012).
76. I. L. Escalante-García, J. S. Wainright, L. T. Thompson, and R. F. Savinell, Performance of a Non-Aqueous Vanadium Acetylacetonate Prototype Redox Flow Battery: Examination of Separators and Capacity Decay, *J. Electrochem. Soc.*, **162**, A363 (2015).